# Stochastic FE analysis of stress concentrations in curved glulam beams due to the uncertainty of material direction

Yu, Taoyi; Khaloian-Sarnaghi, Ani; Seeber, Franziska; van de Kuilen, Jan Willem

**DOI**
10.1016/j.conbuildmat.2023.131537

**Publication date**
2023

**Document Version**
Final published version

**Published in**
Construction and Building Materials

**Citation (APA)**
Yu, T., Khaloian-Sarnaghi, A., Seeber, F., & van de Kuilen, J. W. (2023). Stochastic FE analysis of stress concentrations in curved glulam beams due to the uncertainty of material direction. *Construction and Building Materials*, *393*, Article 131537. https://doi.org/10.1016/j.conbuildmat.2023.131537

Construction and Building Materials 393 (2023) 131537

Contents lists available at ScienceDirect

Construction and Building Materials

journal homepage: www.elsevier.com/locate/conbuildmat

# Stochastic FE analysis of stress concentrations in curved glulam beams due to the uncertainty of material direction

Taoyi Yu [a,*], Ani Khaloian-Sarnaghi [a], Franziska Seeber [a], Jan-Willem van de Kuilen [a,b]

[a] Wood Technology, Department of Materials Engineering, Technical University of Munich, Munich, Germany
[b] Biobased Structures and Materials, Faculty of Civil Engineering and Geosciences, Delft University of Technology, Delft, The Netherlands

ARTICLE INFO

*Keywords:*
Monte-Carlo simulation
Curved glulam
Stress concentration

ABSTRACT

When curved glulam beams are subjected to bending, tension perpendicular to grain is introduced. In this work, Monte-Carlo analysis is conducted to study the influence of the annual-ring orientation of individual board on stress concentration in the radial direction. A virtual cutting program is developed which simulates the sawing processes of boards and yields a database of sawn boards, each with a characterized material direction with respect to the pith location. Lamellas are randomly selected from the database to construct curved glulam beams in FE models for Monte-Carlo simulation. Parameters including lumber diameter distribution, taper function, orthotropic elastic properties are considered for four common wood genera in Europe: spruce, pine, larch, and beech.

Statistical analysis shows that when the annual-ring effect is considered, the average radial stress in the middle height area of the glulam beams can reach up 1.56 times (even higher on the middle width and height area) compared to the common practice, where wood is usually simplified as transverse isotropic material. Such stress concentration, which can trigger early damage of the structure, indicates an underestimation of stress perpendicular to grain in common practice. Moreover, parameter studies show that the stress redistribution depends not only on the mechanical properties of wood species but also on the width of the board layer.

## 1. Introduction

As a natural material used for engineered structures, wood generally builds itself yearly according to the weather cycles, forming annual-rings. Accordingly, wood can be considered cylindrical anisotropic material. In engineering practice, transverse isotropy is commonly considered for wood, that both directions perpendicular to grain are assigned with the same values, which are given for example by Eurocode 5 [1]. However, stiffness and strength are found to vary, for certain species strongly, in radial and tangential directions [2,3]. Hence, the legitimacy of the transverse isotropy assumption should be examined for the structures where stresses perpendicular to grain need to be verified, such as curved glulam.

Glued laminated timber (glulam), often in curved or cambered shape, is widely applied in timber structures. Under bending, tensile stress perpendicular to grain is induced to curved glulam beams (Fig. 1), making the tensile strength perpendicular to grain one of the decisive parameters in such structures [4,5]. Tensile strength, however, is very low in this direction [2]. Consequently, many failure cases under tension perpendicular to grain are observed in the summary work of Franke et al. [6], and many reinforcement measures are designed for this stress, as shown in the works by Blaß et al. [7], Jönsson [8], Fueyo et al. [9]. Extensive experiments on curved glulam beams under short- and long-term loading, in combination with moisture variation can be found in [10,11]. In addition, simulations are conducted to analyze manufacturing stress [12], moisture induced stress [13], and failure [14]. In the FE model by Zhou et al. [15], pith is considered to be located in the bottom center of each board and the resultant stress perpendicular to grain is found to have a saw-toothed pattern, where the maximum stress is higher compared to the case when no annual-ring orientation is implemented. In reality, however, the pith locations of different layers have even higher degree of randomness due to the variability in sawing process, relating to e.g. wood qualities and usages, the variable saw types, and standard practices [16]. This uncertainty, referred as annual-ring effect, is found by this work to cause a non-uniform stress distribution and consequently stress concentrations in curved glulam beams.

Analyzing of stress concentration is important for structural analysis, as it may refer to the area where damage will be initiated. Besides supports, connections, and notches [17,18], stress concentrations in wood material, such as glulam, can also be caused by material inhomogenity, such as the existence of knots [19–22]. To cover the

* Corresponding author.
*E-mail address:* yu@hfm.tum.de (T. Yu).

https://doi.org/10.1016/j.conbuildmat.2023.131537
Received 9 January 2023; Received in revised form 11 April 2023; Accepted 23 April 2023
Available online 13 June 2023

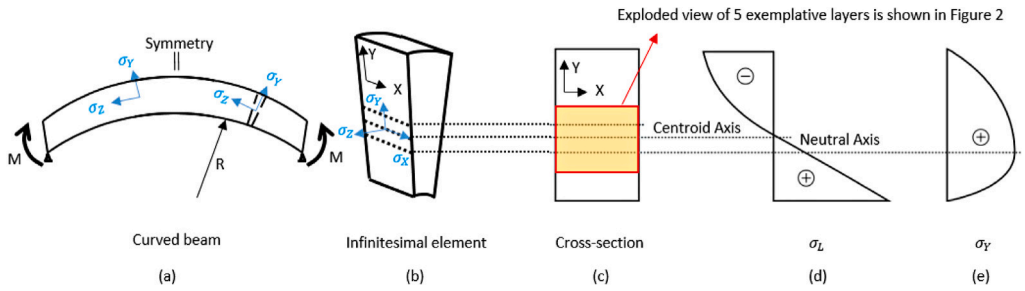


**Fig. 1.** Elastic theory solutions of bending stresses in a curved beam.

influence from inhomogenity, on the one hand, a reduction factor is suggested for estimating the glulam strength, based on e.g. the Weibull's Weakest-Link or Chain Model [23,24]. On the other hand, stochastic models are developed to cover the variability of material property using e.g. the Karlsruher Rechenmodel [25,26], weak zone model [27], or Karhunen–Loève expansion [28]. In addition, uncertainties on the level of finger joints [29], mechanical [30] and moisture load [11] have also been discussed.

This work focuses on studying the uncertainty on the level of the annual-ring setups in different boards of a glulam beam, which has received comparatively little attention so far. A Monte-Carlo analysis is conducted to study the annual-ring effect on distributing the tensile stress to the radial and tangential directions in curved glulam members. In Section 3, a virtual cutting program is generated using PYTHON. The program simulates the sawing processes of logs and yields a database of sawn boards, each with a characterized pith location relative to its board center. This information is implemented into the FE models to generate the material direction of each board through the user subroutine ORIENT of the software ABAQUS in Section 4. Statistical approaches (Section 5) in combination with parameter analysis (Section 6) are adopted to assess the stress concentration level in different species, location inside the glulam, and board dimension.

## 2. Mechanism of stress concentration caused by material direction uncertainty

Different from straight beams, when a curved beam is subjected to bending load (Fig. 1a), besides the stress in the longitudinal direction ($\sigma_L = \sigma_Z$), a perpendicular stress $\sigma_Y$ is triggered, which is in the Y direction of the corresponding cross-section (Fig. 1c). The cause of this stress is that the length of each infinitesimal element is greater in the upper part than in the is lower part due to the beam curvature (Fig. 1b). Consequently, the neutral axis lower than the centroid axis (Fig. 1d), and the largest $\sigma_Y$ occurs below the neutral axis (Fig. 1e).

In order to explain the mechanism of how the $\sigma_Y$ can vary inside the board, Fig. 2 takes 5 layers of boards from the glulam in Fig. 1 as a example, each $i^{th}$ layer with a randomly assigned material rotation angle ($\theta_i$). Due to the bending load, each $i^{th}$ layer exhibits a stress in global Y direction ($\sigma_{Y_{i,gl}}$), which consequently results in strains in global X and Y direction ($\epsilon_{Y_{i,gl}}$, $\epsilon_{X_{i,gl}}$ in Fig. 2b), as can be calculated by Eq. (1):

$$\{\epsilon_{i,gl}\} = [T_{\epsilon_i}][S][T_{\sigma_i}]^{-1}\{\sigma_{i,gl}\} \qquad i = 1, 2, 3... \tag{1}$$

where $[S]$ is the material compliance tensor, $[T_{\epsilon_i}]$ and $[T_{\sigma_i}]$ are the transformation tensors which are functions of the material rotation

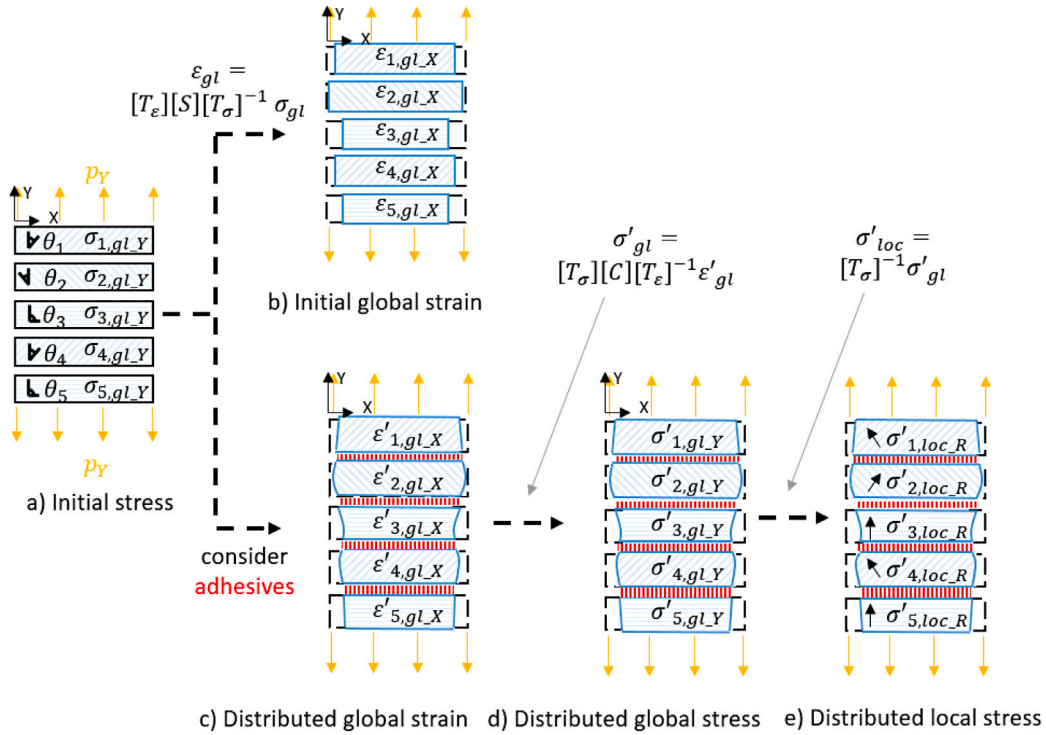


**Fig. 2.** Illustration of stress concentration caused by annual-ring effect using 5 exemplative board layers from Fig. 1.

angles $\theta_i$ (in accordance to annual-rings) of each layer, as shown in Fig. 2a.

Since the rotation angle varies in different layers, the strain in global X direction ($\epsilon_{X_{i,gl}}$) varies, as shown in Fig. 2b. Yet, due to the constraint provided by the adhesives between boards, the strain $\epsilon_{X_{i,gl}}$ difference in neighboring layers is expected to get mitigated, which results in the distributed strain denoted as $\epsilon'_{X_{i,gl}}$ in Fig. 2c. Consequently, the distributed global stress $\sigma'_{i,gl}$ can be calculated by means of Eq. (2):

$$\{\sigma'_{i,gl}\} = [T_{\sigma_i}][C][T_{\epsilon_i}]^{-1}\{\epsilon'_{i,gl}\} \tag{2}$$

where $[C]$ is the material stiffness tensor. Since the distributed strain $\epsilon'_{i,gl}$ differs from the initial strain $\epsilon_{i,gl}$ due to the mitigating effect from the adhesive layers, the distributed stress $\sigma'_{i,gl}$ naturally differs from the initial stress $\sigma_{i,gl}$ as well, both in the global Y and X directions, as shown in Fig. 2d.

In addition to the global stresses, the distributed local stress (Fig. 2e) can be derived as shown in Eq. (3):

$$\{\sigma'_{i,loc}\} = [T_{\sigma_i}]^{-1}\{\sigma'_{i,gl}\} \tag{3}$$

Since the material directions R and $T$ inside each board vary, the distributed stress is also not uniform inside each board. Therefore, stress is much higher in certain locations, which can be considered as stress concentration. The goal of this paper is to use a stochastic FE approach to figure out:

- How severe can be the influence of stress concentration on the mechanical response of the glulam beam?
- At which location does the stress concentration occur and why?
- What are the principal parameters influencing the level of stress concentration?

## 3. Generating material direction uncertainty by virtual cutting program

In order to analyze how the material direction influences the stress distribution in curved glulam, Monte-Carlo simulations are to be performed. For this purpose, the material direction is to be taken as the uncertainty (random variable) and assigned to each individual board. Following the concentric annual-ring assumption, the material direction ($\theta$) of each point (x,y) inside a board can be computed as a function of its relative position to the pith ($x_{pith}$, $y_{pith}$), as shown in Eq. (4). Taking the pith as origin, i.e. $x_{pith} = y_{pith} = 0$, the random variable to be identified becomes the coordinate of the board center ($x_{bc}$, $y_{bc}$). Hence, in this section, the method of using a virtual cutting program to obtain the distribution of this random variable will be explained.

$$\theta = arctan\frac{y - y_{pith}}{x - x_{pith}} \tag{4}$$

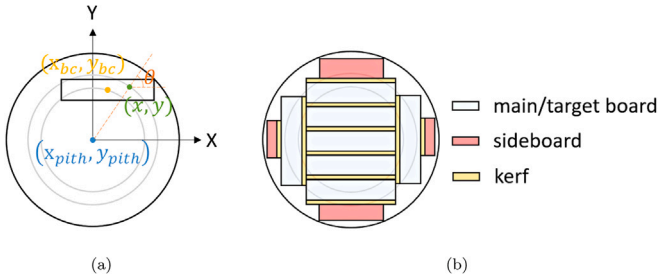


**Fig. 3.** Illustration of: (a) relative pith location; (b) sawing pattern.

Since boards are engineer products, the distribution of the variable ($x_{bc}$, $y_{bc}$) depends highly on the manufacturing process (Fig. 4), including the distribution of the harvested tree size, the distribution of the log diameter, and the sawing patterns.

To simulate this process, a virtual cutting program is developed using Python. Following the four stages indicated in Fig. 4, the program takes the breast-height-diameter (DBH) of harvested trees as the input data, saws them into logs with standard length and classifys them into different classes according to their diameters. A sawing pattern is designed for each class to saw boards out of the logs. Finally, a database of boards is generated, where each board is with a characterized coordinate of its center ($x_{bc}$, $y_{bc}$) relative to the pith.

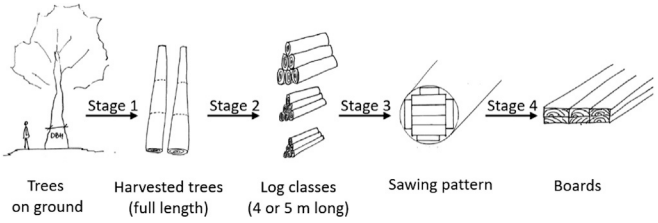


**Fig. 4.** The process of board production.

### Stage 1: Getting the DBH distribution of the harvested trees

Third National Forest Inventory [31] provides the data on the harvest volume of eight different DBH classes of several common harvestable wood genera in Germany from 2002 to 2012. Four of the most commonly applied genera for structural uses in Germany are selected here: spruce, pine, larch, and beech. According to the Kolmogorov–Smirnov test, the data is found to be best fitted with beta distribution and is shown in Fig. 5(a). Accordingly, 10 000 harvested trees are generated as input for the virtual cutting program. The original and simulated data can be seen in Table A.1.

### Stage 2: Getting the diameter distribution of logs and classifying

In this stage, each harvested tree sample (with DBH between 100 mm to 500 mm) is sawn into several logs of length 4 or 5 m. The length is defined in the virtual cutting program as a uniform random variable between 4 and 5 m. The program then calculates for each log its smallest diameter along the log length, as the diameter along each log is not a uniform value but follows an assumed taper. According to the smallest diameter along the length, logs get classified into different classes.

In the assumed tree taper functions, the diameter ($d_h$) at a certain height ($h$) of the tree can be calculated by DBH, the total height of the tress ($H$), and the height ($h$). Moreover, the unknown total tree height can be estimated according to the $H - DBH$ relationship (Fig. 6(a)) provided in literature [32–34]. Afterwards, the tree taper can be generated for each simulated tree, according to its DBH (given in *Stage 1*) and the tree taper function (Fig. 6(b)) provided in literature [35–37].

As a result, 20 000+ (exact value depends on how many logs can be sawn from each tree according to $H - DHB$ relation) logs from the 10 000 harvested tree samples are generated and classified into 20 classes (Table A.2). The diameters of the logs (measured at the end of smaller cross-section) in each class lie between [$d_c$, $d_c + 20$) mm, where $d_c$ is the characteristic diameter of a class.

The fitted beta distributions of log diameter measured at the smaller end are shown in Fig. 5(b). As a result, the mean diameters of all logs measured at the middle height are 251 mm, 233 mm, 221 mm, and 257 mm for spruce, pine, larch, and beech, respectively. The simulated data matches well with a site survey, where the mean log diameters measured at the middle height for spruce, pine, and larch are found to be 246 mm, 225 mm, and 222 mm, respectively.

### Stage 3: Designing sawing pattern for each log class

Boards are sawn out of the logs according to specific sawing patterns, which determine the relative pith location of each board. It is unattainable to cover all possible sawing patterns as they can vary especially in small sawmills from one to another, due to the varying saw types, standard practices, wood qualities and usages [16]. Hence, this work adopts one of the most common sawing patterns, cant-sawing (Fig. 3(b)), which is nowadays being used in large sawmills with

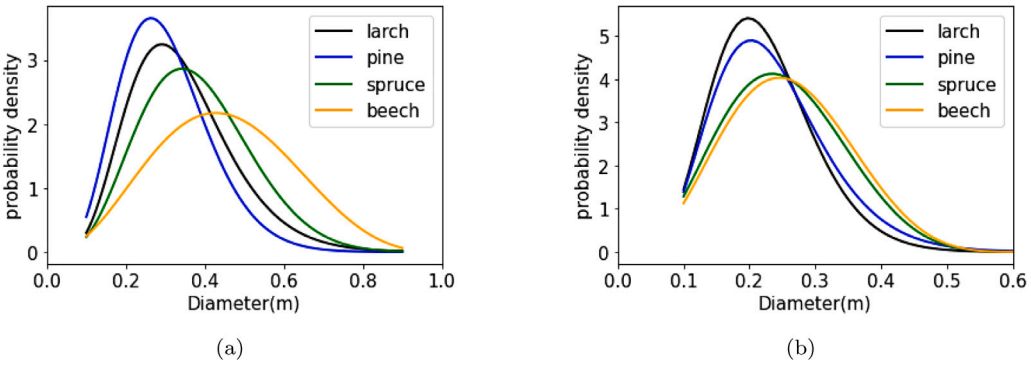


**Fig. 5.** Distribution of: (a) DBH of harvested trees [31] from *Stage 1*; (b) diameter of the logs from *Stage 2*.

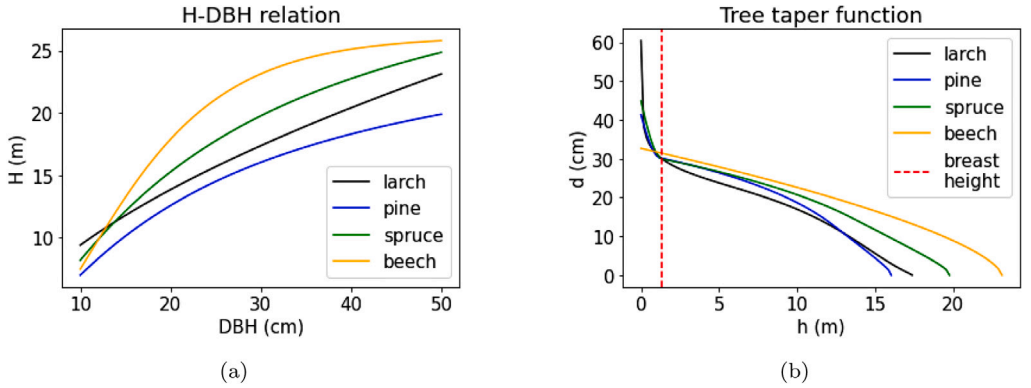


**Fig. 6.** Tree shape: (a) H-DBH relation; (b) tree taper function: example of DBH = 30 cm.

automatic sawing systems. In principle, this approach consists of two steps:

- *Step 1*: saw one or two layers of sideboards, whose dimensions are usually smaller than the targeted boards, out of the four sides, leaving a rectangle middle block;
- *Step 2*: saw the main boards with targeted dimensions out of the rectangle middle block from the previous step.

With respect to this method, a Python program is developed to automatically generate the optimal (in terms of maximum yield) cutting pattern for each class according to the targeted board dimension. The following selecting criteria are adopted:

- the kerf (thickness of the saw) is assumed to be 5 mm thick;
- only the main boards of the targeted dimension are considered;
- when there are multiple sawing patterns, the one with the maximum yield of the targeted boards is chosen;
- for each board dimension, the log classes for sawing are selected by:
  - the yield area should not be smaller than 50% of the log cross-section;
  - the diameter of the log should not be larger than 2 times the targeted board width.

As a result, Table A.3 shows the selected appropriate classes for nine exemplative board dimensions and the corresponding optimal sawing-pattern.

**Stage 4: Generating the database of boards**

In this stage, for each wood genus and board dimension, logs generated at *Stage 2* are sawn according to the patterns designed for each class. As a result, a database of 60 000+ boards with characterized relative pith locations is generated.

As the log diameters in each class lie between $[d_c, d_c + 20)$ mm, the cutting pattern of the class needs to be designed according to characteristic diameter $d_c$, so as to be operable to all logs in this class. Consequently, for all the boards in this class with a diameter ($d$) larger than $d_c$, the cutting pattern can be shifted in any direction by a distance of $d - d_c$. This then results in a shift of pith location for all boards from this log. Therefore, a random shift is added in the virtual cutting program when sawing each log. The shift is assumed to be a vector with the length of $d - d_c$ and the angle $\alpha$, $\alpha$ being a uniform random variable between $[0, \pi]$.

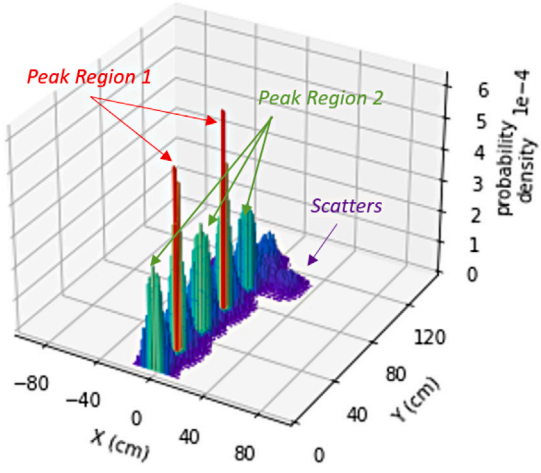


**Fig. 7.** Distribution of the board-center coordinate relative to pith location.

As shown in Table A.3, different log classes and sawing patterns are adopted for each targeted board dimension. Hence, different board dimensions will have different distributions of the board center $(x_{bc}, y_{bc})$.

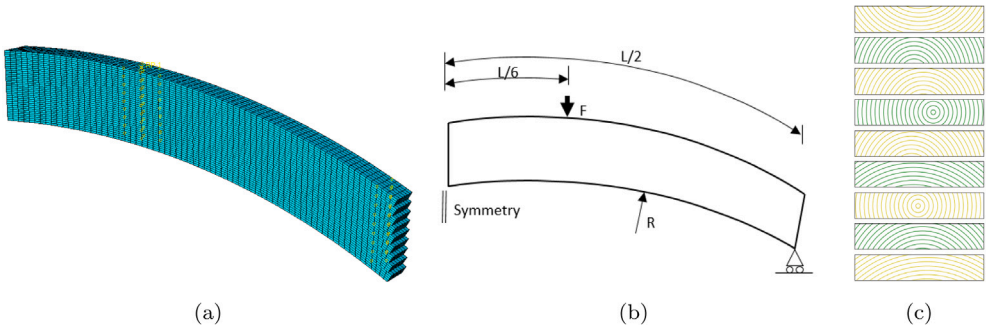


**Fig. 8.** Model information: (a) FEM model; (b) loading and boundary condition; (c) an example of growth ring direction.

As a result, the 3D histograms in Table A.4 summarize the distribution of nine exemplative dimensions of the four wood genera, while Fig. 7 shows the distribution of the relative board center ($x_{bc}$, $y_{bc}$) of 150 × 40 mm spruce boards. Since the distribution is symmetric, only areas of $y > 0$ are plotted. Two main characteristics of the distribution can be observed:

- two main peak regions of the probability density can be identified. The difference in probability density between the two regions becomes subtler as the board thickness decreases.
  - Peak Region 1: $[x \approx 0 \quad , \quad y \approx (n-1)t]$, $\quad n = 1, 2, 3...$
  - Peak Region 2: $\left[x \approx 0 \quad , \quad y \approx (n-\frac{1}{2})t\right]$, $\quad n = 1, 2, 3...$

  where $t$ is the thickness of the board.
- the board centers are concentrated around the line where $x = 0$, except for the ones from far ends in Y directions. These exceptions (marked as *Scatters* in Fig. 7) come from the side boards and have a relatively low occurrence.

Moreover, despite the apparent difference of log-diameter-distribution (Fig. 5(b)) between species for the full diameter range, the log-diameter-distribution inside the range differs not much, neither does the board-center-distribution (Table A.4). This is because that for each targeted board dimension, not all log classes are selected for sawing but only those whose diameter is inside the range that meets the selecting criteria given in *Stage 3*, as can be seen also in Table A.3.

## 4. Parametric FE models

As shown in Section 2, the material direction of the board is essential information for curved glulam modeling and can have a significant impact on stress distribution. In this section, boards are randomly selected from the database generated in Section 3 to construct glulam beams for stochastic FE analysis. By means of Monte-Carlo simulation, the influence of the distribution of pith location on the stress concentration can then be analyzed. 3D FEM models are developed using ABAQUS. Fig. 8 shows the model of the *Test Problem*, where a curved glulam beam with the inner radius of curvature $R = 2862.5$ mm (Fig. 8b) made of 9 layers of 150 × 30 mm board is constructed. The beam is subjected to a four-point bending test. Only half of the beam is modeled due to the symmetry, with a roller support at one end and a symmetrical boundary condition at the apex cross-section. The constraining effect of the adhesives is assumed as tie connection, and the mechanical behavior of the component is studied in the linear elastic range. To avoid the shear-locking under bending, the eight-node brick element with reduced integration (C3D8R) is chosen. Four layers of elements along the thickness direction are assigned for each board layer.

Material parameters of different genera are obtained from literature [38–50] as shown in Table 1.

Besides the *Test Problem*, to study the influence of dimension, different test setups are generated using different combinations of:

- board width: 150 mm, 200 mm, 250 mm;
- board thickness and number of layers: 20 mm × 13 layers, 30 mm × 9 layers, 40 mm × 7 layers;
- material parameters: in Table 1.

For each test setup, a Monte-Carlo analysis is conducted with 300 simulations. The main random variable of each simulation is the pith locations of the boards, which is realized by randomly selecting boards from the database generated in the previously described *Stage 4*. The

**Table 1**
Material parameters of different wood species from literature.

| Species[a] | $E_L$ (e4 MPa) | $E_R$ (e2 MPa) | $E_T$ (e2 MPa) | $\nu_{LR}$ (–) | $\nu_{LT}$ (–) | $\nu_{RT}$ (–) | $G_{LR}$ (e2 MPa) | $G_{LT}$ (e2 MPa) | $G_{RT}$ (e2 MPa) | $\kappa_G$[b] (e–3 1/MPa) | $\kappa_\theta$[b] (–) |
|---|---|---|---|---|---|---|---|---|---|---|---|
| (European) Beech 1 [38] | 1.4 | 19 | 6.1 | 0.86 | 0.28 | 0.23 | 13 | 8.9 | 4.9 | 1.1 | 2.0 |
| (Scots) Pine 1 [39] | 1.4 | 7.0 | 5.5 | 0.03 | 0.04 | 0.38 | 12 | 8.0 | 5.0 | 2.4 | 1.6 |
| (Scots) Pine 2 [40] | 1.0 | 14 | 8.1 | 0.40 | 0.62 | 1.1 | 13 | 13 | 7.4 | 2.2 | 3.0 |
| Pine 3 [41] | 0.69 | 4.5 | 2.7 | 0.38 | 0.39 | 0.46 | 3.5 | 2.6 | 0.34 | 22 | 9.7 |
| (Scots) Pine 4 [42] | 1.5 | 7.6 | 5.3 | 0.60 | 0.74 | 0.69 | 10 | 9.0 | 1.1 | 4.4 | 3.3 |
| Spruce 1 [43] | 1.4 | 9.1 | 4.9 | 0.45 | 0.54 | 0.56 | 7.4 | 5.1 | 0.33 | 26 | 24 |
| (Norway) Spruce 2 [44] | 1.6 | 7.0 | 4.0 | 0.019 | 0.013 | 0.24 | 6.3 | 7.8 | 0.37 | 22 | 16 |
| (Norway) Spruce 3 [45] | 1.2 | 8.3 | 4.9 | 0.041 | 0.033 | 0.35 | 7.0 | 6.6 | 0.66 | 11 | 9.2 |
| (Norway) Spruce 4 [46] | 1.2 | 8.2 | 4.2 | 0.056 | 0.035 | 0.31 | 7.4 | 6.2 | 0.42 | 20 | 16 |
| (Norway) Spruce 5 [41] | 1.3 | 6.3 | 4.0 | 0.36 | 0.45 | 0.33 | 6.2 | 5.9 | 0.53 | 14 | 8.6 |
| (Western) Larch 1 [47] | 1.3 | 10 | 8.4 | 0.36 | 0.28 | 0.39 | 8.1 | 8.9 | 0.90 | 8.2 | 8.3 |
| (Chinese) Larch 2 [48] | 0.76 | 7.7 | 3.6 | 0.22 | 0.30 | 0.77 | 4.3 | 3.9 | 4.5 | 3.8 | 3.0 |
| (Chinese) Larch 3 [49] | 0.99 | 8.5 | 4.8 | 0.41 | 0.023 | 0.41 | 6.3 | 2.3 | 7.7 | 2.9 | 2.5 |
| (Dahurian) Larch 4 [50] | 1.7 | 12 | 11 | 0.37 | 0.49 | 0.53 | 6.2 | 3.4 | 0.55 | 16 | 19 |

[a]Considering the measuring accuracy, all numbers are rounded to 2 scientific digits.

[b]$\kappa_G$ and $\kappa_\theta$ are calculated based on the 9 engineering constants and are explained in Section 6.

material directions (radial $R$, tangential $T$, and longitudinal $L$) of each layer are implemented using a user subroutine, ORIENT, such that:

- the longitudinal direction follows the length direction of each board;
- the radial and tangential directions of each layer are determined by the relative location of the board center to the pith;
- with respect to the common practice, the boards are flipped so that except for the top layer, the relative pith locations of all other layers are below their respective board centers.

## 5. Result interpretation method

### 5.1. Qualititive overview

Fig. 9 shows five simulation examples of the *Test Problem* using the material parameters of *Spruce 1* in Table 1. The white lines indicate the annual rings of each board. Simulation number 0 (abbreviated as *Sim0*) is the *Standard Case* where for all the layers, the global Y and X directions are considered as local radial and tangential directions, respectively. *Sim1* to *Sim4* are four examples where the boards are randomly selected from the generated database in Section 2 *Stage 4*.

In Fig. 9(a), for the *Standard Case* (*Sim0*), the simulated local radial stress $\sigma_R^{'}$ with the maximum value 1.12 MPa at around middle height (marked with **X** in the figures) is consistent with the analytical solution of $\sigma_Y$, since the local R direction and the global Y direction coincide in *Sim0*.

After assigning the uncertainty of material direction, i.e. variation of the material properties with respect to the random pith location of each layer in a cylindrical coordinate system, the stresses perpendicular to grain get distributed. As shown in *Sim2*, the maximum value can reach up to 2.19 MPa. Similarly in Fig. 9(b), the almost zero-valued tangential stress $\sigma_T^{'}$ in the *Standard Case* gets distributed so that it reaches a value as high as 1.76 MPa, shown in *Sim4*.

### 5.2. Statistical analyze of stress concentration factor $SCF$

As shown in Fig. 10b, the mesh in the cross section of each board layers contains 24 C3D8R elements, giving 24 integration points. After simulation, the stresses on the full cross-section (Fig. 10a) are obtained by interpolating the values of the integration points. To get a statistical view of the stress distribution across the cross-section, a histogram of stress values of the 24 integration points in multiple simulation cases is plotted, as shown in Fig. 10c. This histogram indicates the occurrence frequency of stress levels in the cross-section of a board layer. In the following, through 300 simulations, 7200 stress values are taken to build the stress histogram for each layer, giving a stable estimate of the mean stress (shown by a red line) and 95-percentile stress (shown by a yellow line). Moreover, in order to compare with the case where random annual-ring is not considered, the stress of *Standard Case* is marked by a green line.

Fig. 11(a) shows the histograms of local radial stress $\sigma_R^{'}$ of the *Test Problem* using the material parameters of *Spruce 1*. As can be seen,

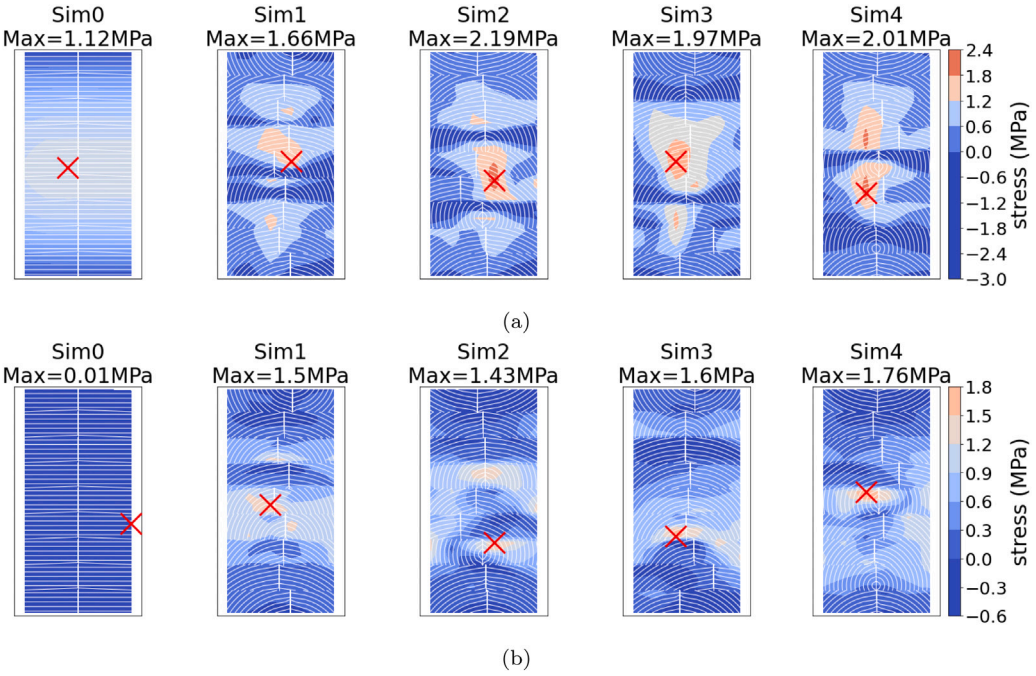


**Fig. 9.** Stress development in the cross-section at the middle length of the glulam of the *Test Problem*: (a) local redistributed radial stress $\sigma_R^{'}$; (b) local redistributed tangential stress $\sigma_T^{'}$.

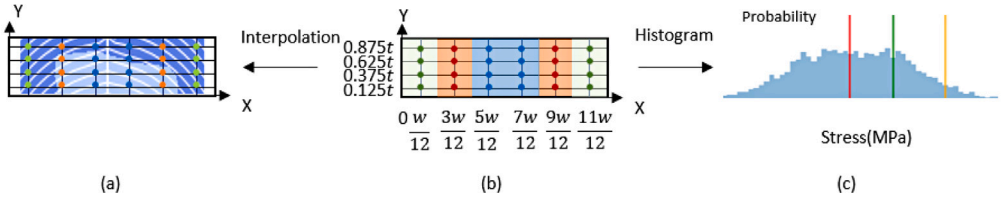


**Fig. 10.** Method of analysis of the stress results from integration points ($t$ and $w$ represent the thickness and width of the board, respectively). (For interpretation of the references to color in this figure legend, the reader is referred to the web version of this article.)

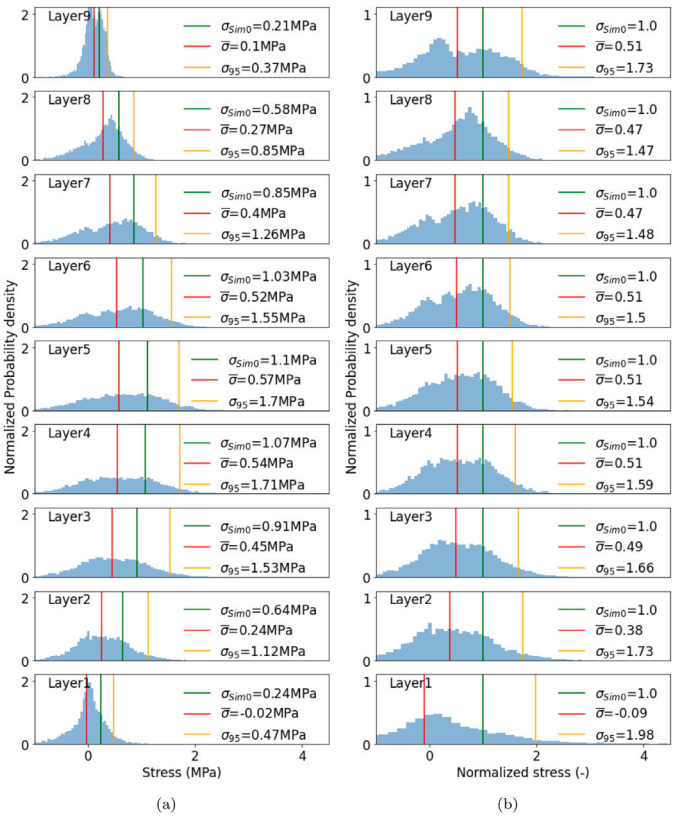


**Fig. 11.** Example of stress histograms of *Test Problem* for all layers using *Spruce 1* from Table 1: (a) local redistributed radial stress $\sigma_R^{'}$; (b) normalized radial stress.

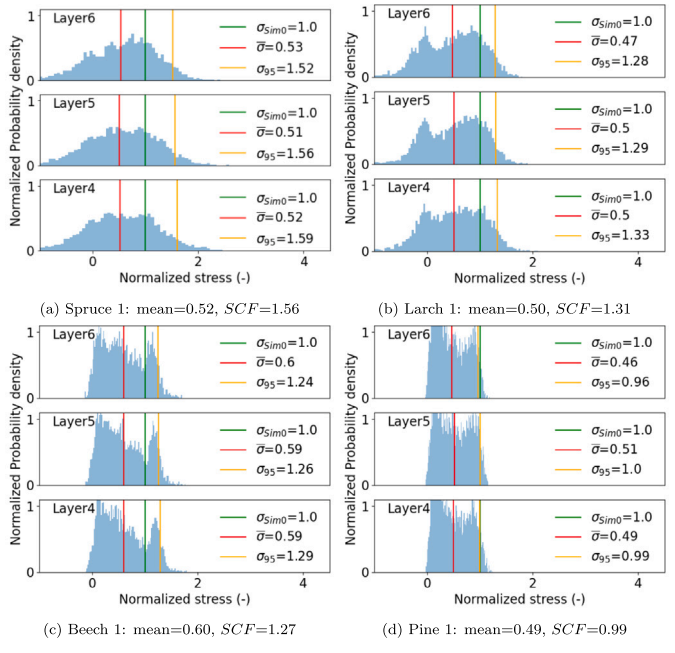


**Fig. 12.** Histograms of local distributed radial stress $\sigma_R^{'}$ in *Middle* $\frac{1}{3}$ of *Test Problem* using different species.

for each layer, the mean stress is lower than the stress calculated by the *Standard Case*, while the 95-percentile is larger. Across the whole height of the beam, the stress follows a parabolic curve, such that the maximum is around the middle height (Layer 5).

In order to better visualize the distribution characteristics, another histogram is generated in Fig. 11(b) using the normalized stress with respect to the *Standard Case*. This normalized stress at each integration point of each simulation case is calculated by dividing the simulated stress in this case by the stress of this point in the *Standard Case* (*Sim0*).

As a result, it can be seen that the middle 3 layers in *Test Problem* (i.e., *Middle* $\frac{1}{3}$ in the thickness direction of the beam) share almost the same distribution for the normalized stress. Since the *Middle* $\frac{1}{3}$ is also the region, where the curved glulam beam is most stressed in the perpendicular to grain direction, this region is considered as the main focus of this paper and the following results will mainly be shown for the *Middle* $\frac{1}{3}$. Moreover, the average 95-percentile normalized stress for the *Middle* $\frac{1}{3}$ is considered as the stress concentration factor, $SCF$. This parameter indicates how much the stress gets amplified in the critical *Middle* $\frac{1}{3}$.

## 6. Parameter study

### 6.1. Influence of species

Fig. 12 shows the distributed radial stress of four species using the material parameters from Table 1. It can be seen that the shape of the histogram, as well as the value of $SCF$, varies in each case. The distribution is not symmetric, and in most cases, there is more than one peak of probability density.

Table 2 summarizes the mean normalized stresses and the 95-percentile normalized stresses ($SCF$) for all the materials given in Table 1. The mean normalized stresses for all species lie between 0.48 to 0.60, while $SCF$ vary from 0.99 to 1.56.

However, for each wood genus, different material parameter values are found in different research works as shown in Table 1. Hence, for each wood genus, the computed $SCF$ according to the Monte-Carlo simulations varies. The widest variation is observed by larch, from 0.99 to 1.46. This is because the parameters are taken from three different larch species (i.e. Dahurian, China, and Western Larch) due to the lack of data on European Larch.

In general, spruce (primarily Norway Spruce) yields the largest $SCF$, from 1.37 to 1.56, while pine (primarily Scots Pine) yields a lower range of $SCF$, from 0.99 to 1.38. For beech, according to the single source (European Beech) found by the authors, the $SCF$ equals 1.27.

To explain the difference of $SCF$ of different species, two possible factors can be identified:

- *Factor 1*: the difference between the pith-location distribution;
- *Factor 2*: the difference between material parameters.

In order to see how strong the influence of *Factor 1* is, another simulation set is carried out, where 14 same materials from the 4 wood genera (beech, spruce, pine, larch), as presented in Table 1, are used. However, in this case, instead of using 4 different pith-location distributions corresponding to the 4 genera, the pith-location distribution of beech is applied for all genera. The results are shown in Table 2. As stated in Section 3, the difference in pith location distribution between the four genera is small. It can also be seen from Table 2 that the influence of *Factor 1* is not significant, thus the primary influence on the final stress distribution should come from *Factor 2*, the material parameters.

**Table 2**
*SCF* and *mean* of different species from Test Problem.

| Species | With correspondent pith distribution | | With pith distribution of beech | |
|---|---|---|---|---|
| | $SCF$ $(\sigma_{95})$ | *mean* $(\overline{\sigma})$ | $SCF$ $(\sigma_{95})$ | *mean* $(\overline{\sigma})$ |
| (European) Beech 1 [38] | 1.27 | 0.60 | 1.27 | 0.60 |
| (Scots) Pine 1 [39] | 0.99 | 0.50 | 0.99 | 0.52 |
| (Scots) Pine 2 [40] | 1.21 | 0.57 | 1.20 | 0.59 |
| Pine 3 [41] | 1.38 | 0.49 | 1.42 | 0.53 |
| (Scots) Pine 4 [42] | 1.25 | 0.51 | 1.27 | 0.55 |
| Spruce 1 [43] | 1.55 | 0.51 | 1.59 | 0.53 |
| (Norway) Spruce 2 [44] | 1.46 | 0.52 | 1.48 | 0.52 |
| (Norway) Spruce 3 [45] | 1.39 | 0.53 | 1.41 | 0.53 |
| (Norway) Spruce 4 [46] | 1.49 | 0.53 | 1.51 | 0.53 |
| (Norway) Spruce 5 [41] | 1.37 | 0.53 | 1.39 | 0.53 |
| (Western) Larch 1 [47] | 1.31 | 0.49 | 1.34 | 0.52 |
| (Chinese) Larch 2 [48] | 1.18 | 0.56 | 1.15 | 0.58 |
| (Chinese) Larch 3 [49] | 0.99 | 0.51 | 0.98 | 0.52 |
| (Dahurian) Larch 4 [50] | 1.46 | 0.48 | 1.53 | 0.51 |

### 6.2. Influence of location

From the observation of Fig. 9a, the maximum distributed radial stress (marked with X in the figure) is exhibited mainly in the *Middle* $\frac{1}{3}$ of the vertical direction, as well as in the center part of the horizontal direction. Hence, according to the arrangement of the integration points shown in Fig. 10b (presented by color code), three different regions can be classified for each cross-section, namely the blue (the center $\frac{1}{3}$ of horizontal direction), green (the two outermost 1/6 from both sides), and orange regions.

Fig. 13 shows the histograms of the normalized stress of these three regions under *Test Problem* using the material parameters of *Spruce 1*. As can be seen, the $SCF$ for the outermost green region is only 0.92. The $SCF$ reaches 1.78 in the center blue region (referred to as $SCF_{center}$ in the following). Compared to the $SCF$ for the whole region which equals 1.55 as shown in Fig. 12a, $SCF_{center}$ is also much higher. The same phenomenon is also observed in other species, confirming that the center blue region is, in general, the most critical area.

This phenomenon is related to the feature that the pith location is mainly located around the center line of the board, as explained in Section 3 and shown in Fig. 7. This feature results in the largest material direction difference between neighboring layers always exhibited around the center line (can be observed in Fig. 9), which consequently leads to the strongest stress concentration.

### 6.3. Influence of board dimension

In addition to the locational influence presented in the previous paragraphs, in this part, the influence of the board width and thickness on the $SCF$ is analyzed.

Fig. 14 shows the histogram of the normalized stress of the glulam beams made of boards with different thicknesses and widths. It can be concluded that:

- no dependency of $SCF$ on the thickness can be observed;
- $SCF$ decreases by increasing the width.

Such observations can be explained: as illustrated in Section 2, the major cause of the $SCF$ is the deviation of the distributed strain in X direction, due to the material direction deviation between different layers. Since the area around the pith exhibits the most severe material orientation change, the smaller the width, the larger the influence from this pith-region, consequently the larger the $SCF$ value.

## 7. Identification of principal parameters $\kappa_G$ and $\kappa_\theta$

Knowing that the material parameters are the main factor influencing the $SCF$ of a certain species, it is useful to identify one principal parameter (from the 9 engineering constants) that can give a direct indication of the magnitude $SCF$.

Recalling the mechanism explained in Section 2 Fig. 2, the main cause of the stress distribution is the deviation of initial X direction strain ($\epsilon_X$ from Eq. (1)) in different board layers. Hence, the first step to find the principal parameter is to identify the parameter that dominates $\epsilon_X$.

As the longitudinal stress has a minor influence on the stress distribution in the perpendicular to grain direction, Eq. (1) can be simplified and reformulated in the form of Eq. (5):

$$\begin{Bmatrix}\epsilon_X\\ \epsilon_Y\\ \epsilon_{XY}\end{Bmatrix} = [T_{\epsilon_i}][S][T_{\sigma_i}]^{-1}\begin{Bmatrix}\sigma_X\\ \sigma_Y\\ \sigma_{XY}\end{Bmatrix} = [S']\begin{Bmatrix}0\\ p_Y\\ 0\end{Bmatrix} \tag{5}$$

Since $\sigma_X$ and $\sigma_{XY}$ are ignorable, the initial strain in X direction ($\epsilon_X$) is mainly influenced by the loading from Y direction ($p_Y$) and can be derived as:

$$\epsilon_X = S'_{RT} p_Y \tag{6}$$

such that $\epsilon_X$ is controlled by the component $S'_{RT}$ of the transformed compliance tensor $[S']$ and can be represented as:

$$S'_{RT} = \frac{-\nu_{RT}}{E_R} + \cos^2\theta\sin^2\theta\left(\frac{E_R + E_T + 2\nu_{RT}E_T}{E_R E_T} - \frac{1}{G_{RT}}\right) \tag{7}$$

By replacing the term $\frac{E_R E_T}{E_R+E_T+2\nu_{RT}E_T}$ in Eq. (7) with a new material parameter called $G_{optimal}$, the above equation turns to:

$$S'_{RT} = \frac{-\nu_{RT}}{E_R} + \cos^2\theta\sin^2\theta\left(\frac{1}{G_{optimal}} - \frac{1}{G_{RT}}\right) \tag{8}$$

This parameter is named "optimal" here, because Eq. (8) turns to its simple configuration (presented in Eq. (9)), when the rolling shear modulus $G_{RT}$ equals $G_{optimal}$:

$$S'_{RT} = \frac{-\nu_{RT}}{E_R} \tag{9}$$

A particular case where $G_{RT} = G_{optimal}$ is the transverse isotropic material. This means that the component $S'_{RT}$ is a constant in this case. Hence, according to Eq. (6), $\epsilon_X$ is independent of the rotation angle $\theta$. In such case, in Fig. 2b, the deviation of the global strain $\epsilon_{Xi}$ will not be amplified by the deviation of material directions. Consequently, this results in the optimal result where the final distributed global stresses remain the same as the initial global stresses, no matter how different the rotation angles of the different layers are:

$$\{\sigma'_i\} = \{\sigma_i\} \tag{10}$$

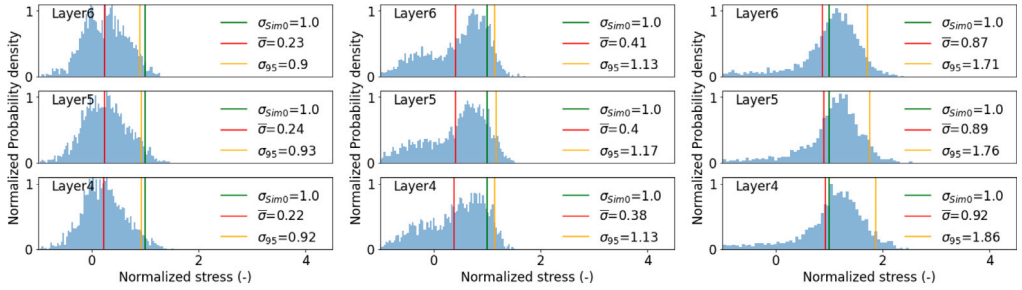


(a) green region, $SCF$=0.92 (b) orange region, $SCF$=1.15 (c) blue region, $SCF$=1.78

**Fig. 13.** Histograms of redistributed radial stress of *Test Problem* using *Spruce 1* in different regions. (For interpretation of the references to color in this figure legend, the reader is referred to the web version of this article.)

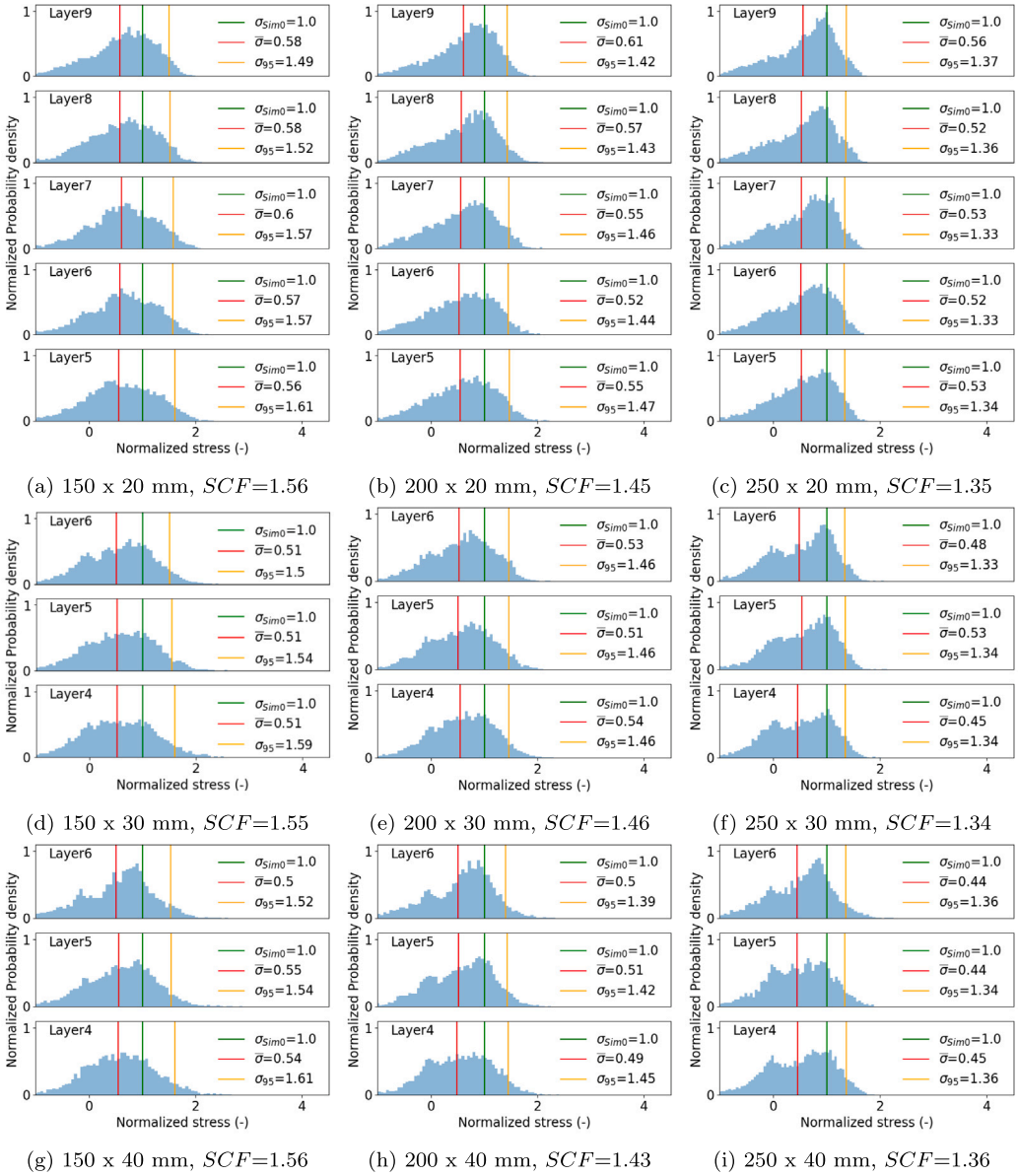


(a) 150 x 20 mm, $SCF$=1.56 (b) 200 x 20 mm, $SCF$=1.45 (c) 250 x 20 mm, $SCF$=1.35

(d) 150 x 30 mm, $SCF$=1.55 (e) 200 x 30 mm, $SCF$=1.46 (f) 250 x 30 mm, $SCF$=1.34

(g) 150 x 40 mm, $SCF$=1.56 (h) 200 x 40 mm, $SCF$=1.43 (i) 250 x 40 mm, $SCF$=1.36

**Fig. 14.** Histogram of redistributed radial stress for different dimensions.

From Eq. (8), a principal material parameter can be identified as $\kappa_G$, such that:

$$\kappa_G = |\frac{1}{G_{optimal}} - \frac{1}{G_{RT}}| \tag{11}$$

$\kappa_G$ is an indicator of how much of the excessive strain $\delta\epsilon_X^{'}$ is caused by the material rotation, i.e.:

$$\delta\epsilon_X' = f\left(\kappa_G\right) \tag{12}$$

To verify the correlation between $\kappa_G$ and $SCF$, 14 Monte-Carlo simulations are conducted for the 14 species listed in Table 1. For each species, 300 simulations are carried out for the *Test Problem*. As a result, Fig. 15(a) shows the relation between $\kappa_G$ and $SCF$. Through linear regression, a coefficient of determination ($R^2$) of 0.71 can be obtained.

However, although $\kappa_G$ is the main parameter influencing the excessive strain, the distributed stress in the R direction is influenced by more factors. Hence, in the following, another principal parameter $\kappa_\theta$ is identified, taking into consideration the mechanism of how the excessive strain results in stress distribution.

According to the constitutive law (Eqs. (2) and (3)), the distributed local stresses can be calculated by:

$$\{\sigma_{local}'\} = [C][T_{\epsilon_i}]^{-1}\{\epsilon_{global}'\} \tag{13}$$

The additional radial stress caused by the excessive strain $\delta\epsilon_X^{'}$:

$$\begin{aligned}\delta\sigma_R' &= \left(\frac{E_R}{1-\nu_{RT}\nu_{TR}} - \sin^2\theta\frac{E_R(\nu_{TR}-1)}{1-\nu_{RT}\nu_{TR}}\right)\delta\epsilon_X' \\ &= \left(\frac{E_R}{1-\nu_{RT}\nu_{TR}} - \sin^2\theta\kappa_2\right)\delta\epsilon_X'\end{aligned} \tag{14}$$

where $\kappa_2 = \frac{E_R(\nu_{TR}-1)}{1-\nu_{RT}\nu_{TR}}$.

Moreover, as shown in Eq. (12), for a given $\theta$, $\delta\epsilon_X^{'}$ is function of $\kappa_G$. Therefore, the $\delta\sigma_R^{'}$ can be expressed as:

$$\delta\sigma_R' = f(\kappa_2, \delta\epsilon_X') = f(\kappa_2, \kappa_G) \tag{15}$$

Hence, the parameter $\kappa_2$ together with $\kappa_G$ leads to a new dimensionless parameter, which is denoted as $\kappa_\theta$ and is presented in Eq. (16):

$$\kappa_\theta = \left|\frac{E_R(\nu_{TR}-1)}{1-\nu_{RT}\nu_{TR}}\left(\frac{1}{G_{optimal}} - \frac{1}{G_{RT}}\right)\right| = |\kappa_2\kappa_G| \tag{16}$$

As a result, Fig. 15(b) shows the relationship between $\kappa_\theta$ and $SCF$. Through linear regression, a higher coefficient of determination ($R^2$) of 0.76 compared to the one from $\kappa_G$ (Fig. 15(a)) can be obtained.

Moreover, the correlation between $SCF_{center}$ and the two parameters ($\kappa_G$ and $\kappa_\theta$) is shown in Fig. 16. Similarly, both show good correlation with $SCF_{center}$, wihle the $\kappa_\theta$ can be a better indicator.

## 8. Conclusions

In this work, a virtual cutting program combined with Monte-Carlo analyses, which consider the uncertainty on the level of material

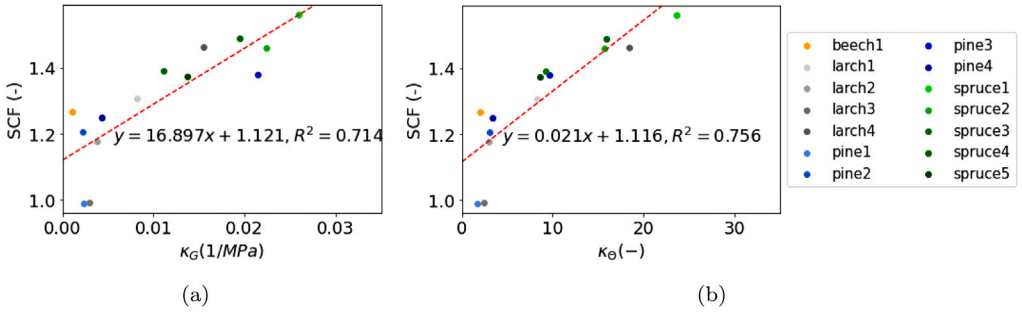


**Fig. 15.** Relation between $SCF$ of *Test Problem* and the parameter: (a) $\kappa_G$; (b) $\kappa_\theta$.

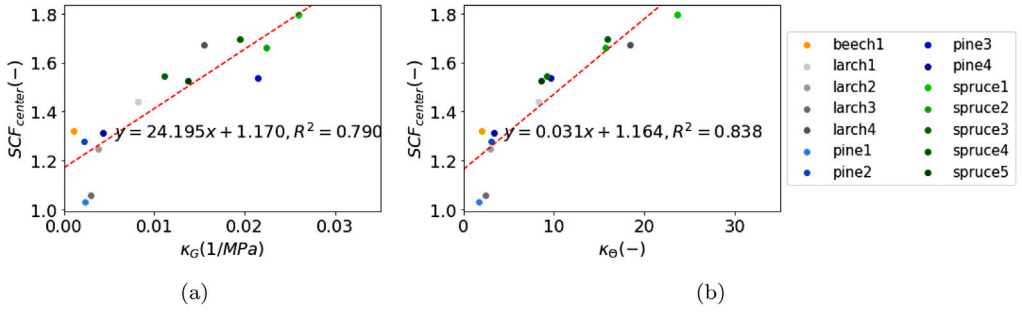


**Fig. 16.** Relation between $SCF_{center}$ of *Test Problem* and the parameter: (a) $\kappa_G$; (b) $\kappa_\theta$.

directions of different board layers, is conducted to analyze the annual-ring effect on stress concentration perpendicular to grain inside curved glulam beams. Based on the *Test Problem* using the material parameters of four wood genera (each contains one or more species from different research works), the stress perpendicular to grain can be up to 78% higher than what engineers usually estimate, as the difference of material parameters in radial and tangential directions is not considered in common engineering practices or in Eurocode 5 [1].

The cause of the stress concentration in this study is identified to be the anisotropy (cylindrical orthotropy as assumed here) of wood material, which triggers the deviation of strain in the width direction of the beam between different board layers and consequently the stress concentration.

In addition, by means of the parameter study, three major features can be observed:

- Dependence on the species: due to the difference in elastic material parameters, different species exhibit different $SCF$. In general, spruce has a high $SCF$ compared to pine and beech. Moreover, the material parameters $\kappa_G$ and $\kappa_\theta$ are found to be good indicators of $SCF$.
- Dependence on the location: due to the cutting patterns, the pith of each board occurs most frequently around the center vertical line of the cross-section, making this region the most critical part as there exhibits the highest $SCF$.
- Dependence on the dimension: the $SCF$ is negatively correlated with the width of the board, yet independent of the thickness.

Accordingly, the following insights can be brought to stress optimization in curved glulam production:

- $\kappa_G$ and $\kappa_\theta$ can be good indicators of whether a wood species is preferable for curved-gluam production.
- To avoid the high $SCF$ in the center of the cross-section, manufacturers can:
  - select the boards whose pith is not located around the center vertical line to be used for the middle layers of a glulam.
  - cut the boards from logs of larger diameter, so as to yield boards with more scattered pith distribution.
- $SCF$ analysis should be conducted especially when producing curved glulam beams of small width.

## CRediT authorship contribution statement

**Taoyi Yu:** Methodology, Software, Writing – original draft, Writing – review & editing. **Ani Khaloian-Sarnaghi:** Conceptualization, Methodology, Writing – review & editing, Supervision, Project administration, Funding acquisition. **Franziska Seeber:** Methodology, Software, Writing – review & editing. **Jan-Willem van de Kuilen:** Conceptualization, Writing – review & editing, Supervision, Project administration, Funding acquisition.

## Declaration of competing interest

The authors declare that they have no known competing financial interests and personal relationships that could have appeared to influence the work reported in this paper.

## Data availability

Part of the data can be made available on request.

## Acknowledgments

The authors gratefully acknowledge the support of the German Research Foundation (DFG) through TUM International Graduate School of Science and Engineering (IGSSE), GSC 81 for funding the project FaiMONat, which allowed for the work presented in this paper.

Additional funding was received from Federal Ministry of Food and Agriculture in FKZ: 22009817 "HS-Hybrid" project, and Bayerische Staatsministerium für Ernährung, Landwirtschaft und Forsten for the Project G2/N/19/05 "EasyBeech", which partly supported the work of this paper.

## Appendix

See Tables A.1–A.4.

**Table A.1**
Distribution of DBH.

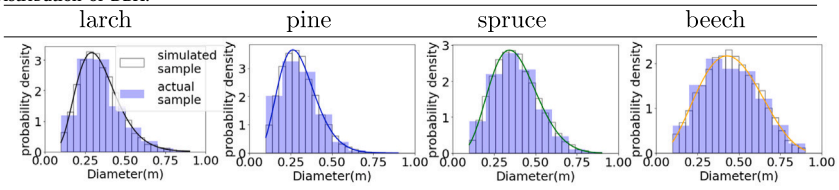


**Table A.2**
Distribution of log diameters.

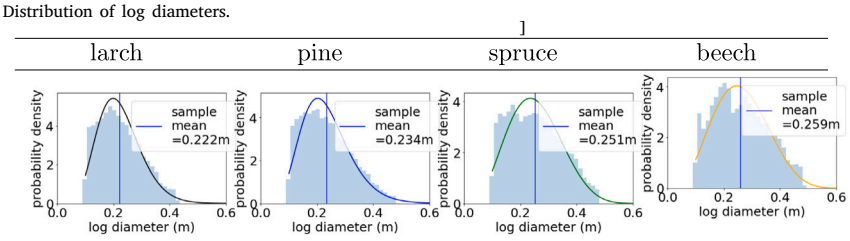

**Table A.3**
Sawing patterns.

| |
|---|
| Board Dimension: 150x40 mm<br>($d_c$ of selected log-classes: 220, 240, 260, 280, 300, 320) |
| 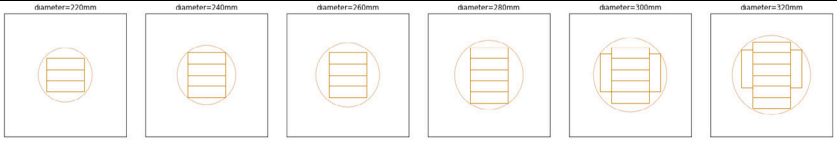 |
| Board Dimension: 150x30 mm<br>($d_c$ of selected log-classes: 200, 220, 240, 260, 280, 300) |
| 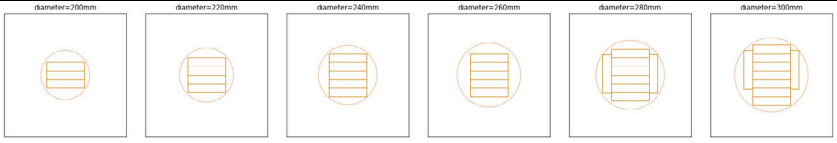 |
| Board Dimension: 150x20 mm<br>($d_c$ of selected log-classes: 200, 220, 240, 260, 280, 300) |
| 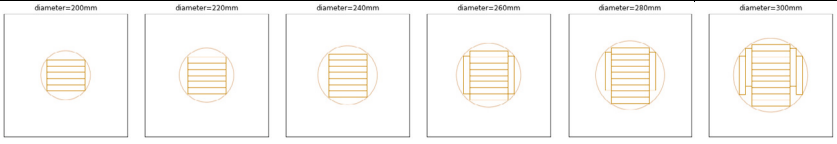 |
| Board Dimension: 200x40 mm<br>($d_c$ of selected log-classes: 260, 280, 300, 320, 340, 360, 380, 400) |
| 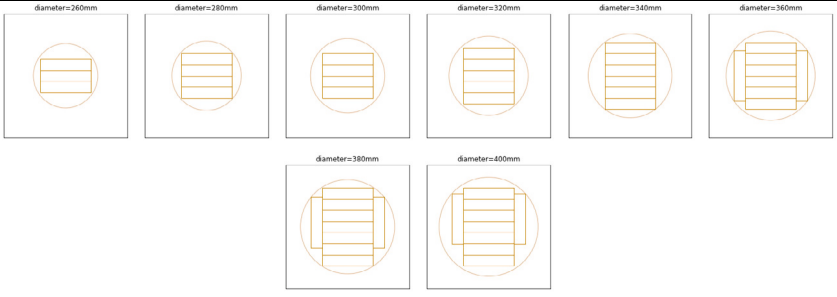 |
| Board Dimension: 200x30 mm<br>($d_c$ of selected log-classes: 260, 280, 300, 320, 340, 360, 380, 400) |
| 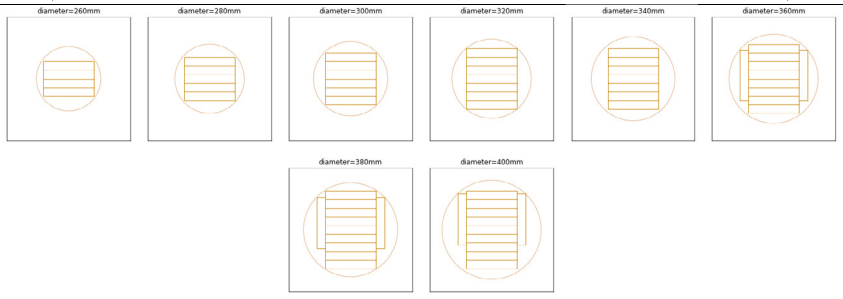 |

(*continued on next page*)

**Table A.3** (*continued*).

| |
|---|
| Board Dimension: 200x20 mm<br>($d_c$ of selected log-classes: 260, 280, 300, 320, 340, 360, 380, 400) |
| 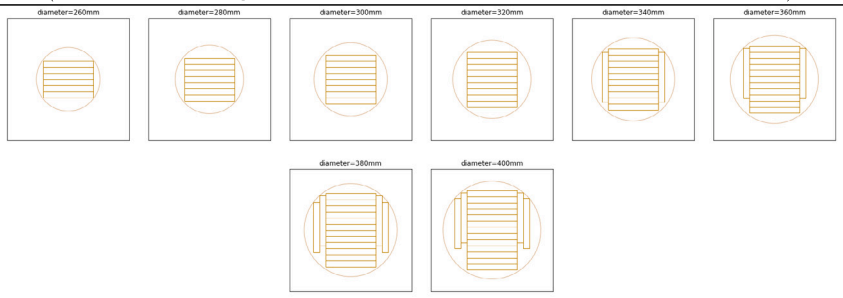 |
| Board Dimension: 250x40 mm<br>($d_c$ of selected log-classes: 320, 340, 360, 380, 400, 420, 440, 460, 480) |
| 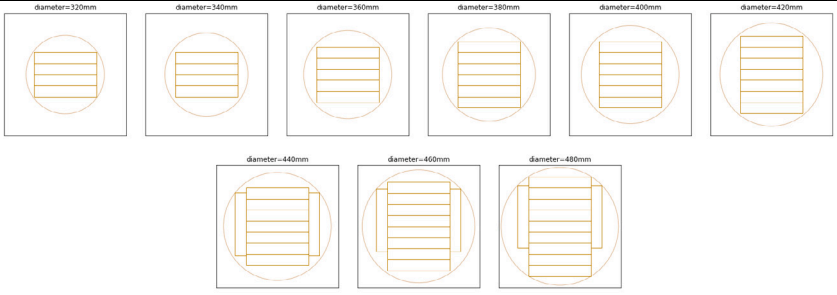 |
| Board Dimension: 250x30 mm<br>($d_c$ of selected log-classes: 300, 320, 340, 360, 380, 400, 420, 440, 460, 480) |
| 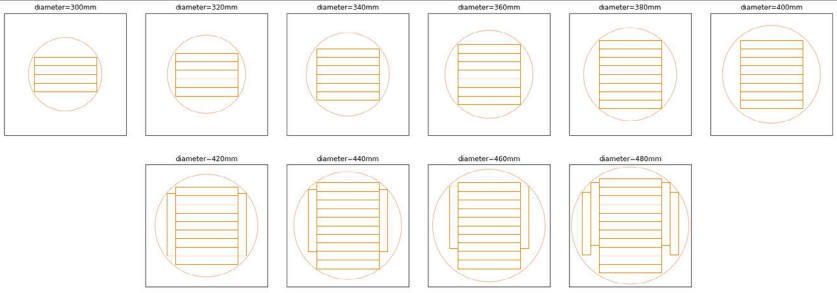 |
| Board Dimension: 250x20 mm<br>($d_c$ of selected log-classes: 300, 320, 340, 360, 380, 400, 420, 440, 460, 480) |
| 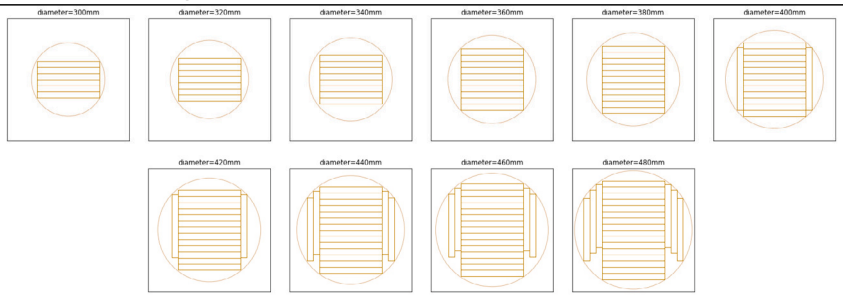 |

**Table A.4**
Scatter of the board-center coordinate in relative to pith.

| board size | larch | pine | spruce | beech |
|---|---|---|---|---|
| 250 x 40 mm | 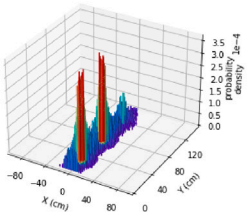 | 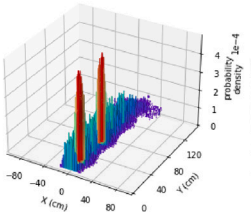 | 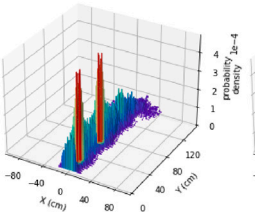 | 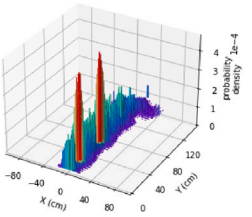 |
| 250 x 30 mm | 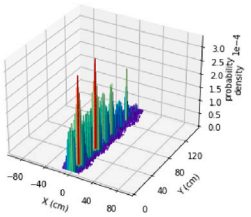 | 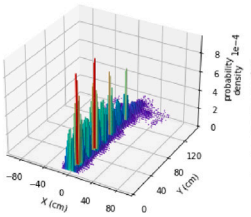 | 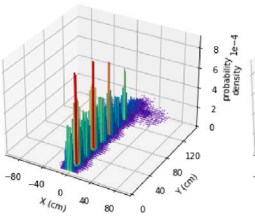 | 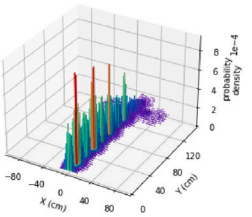 |
| 250 x 20 mm | 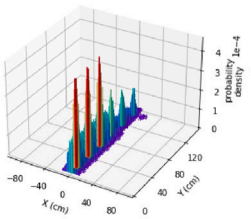 | 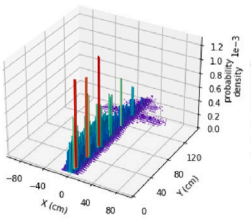 | 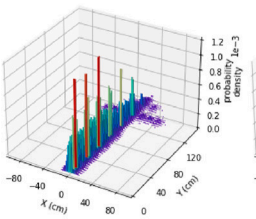 | 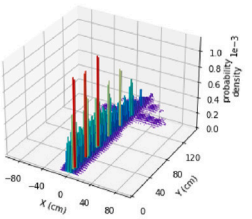 |
| 200 x 40 mm | 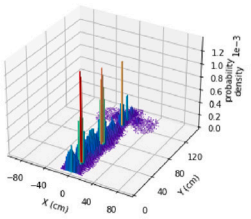 | 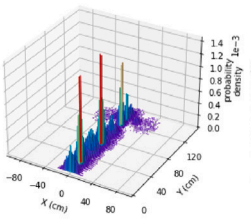 | 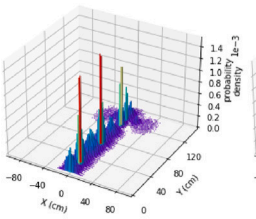 | 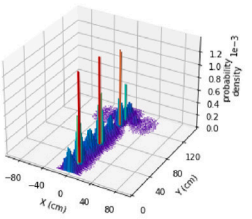 |
| 200 x 30 mm | 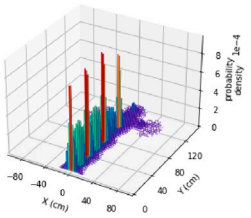 | 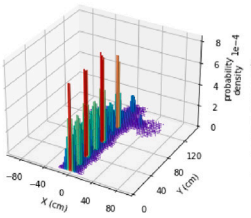 | 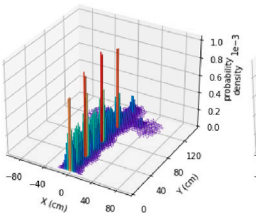 | 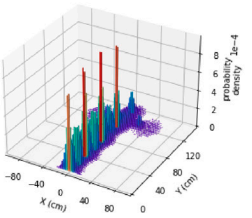 |
| 200 x 20 mm | 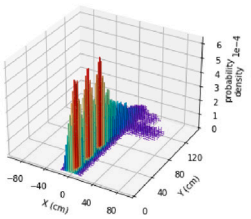 | 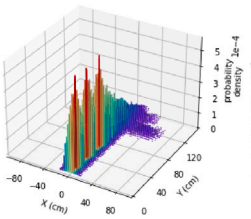 | 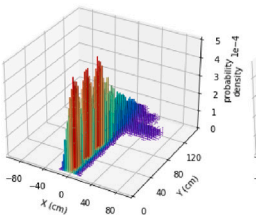 | 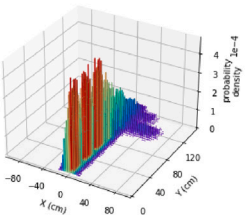 |

(*continued on next page*)

**Table A.4** (*continued*).

| | | | | |
|---|---|---|---|---|
| 150 x 40 mm | 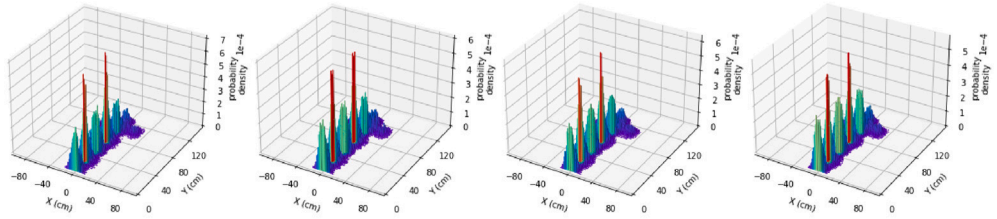 | | | |
| 150 x 30 mm | 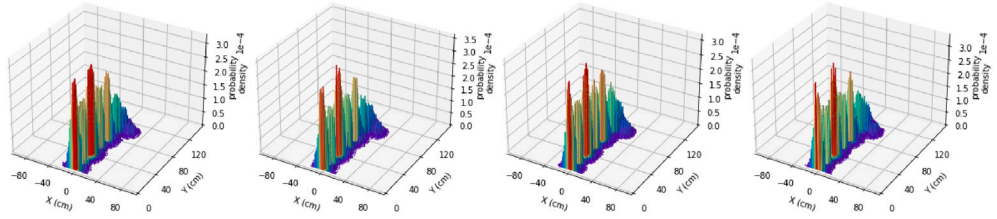 | | | |
| 150 x 20 mm | 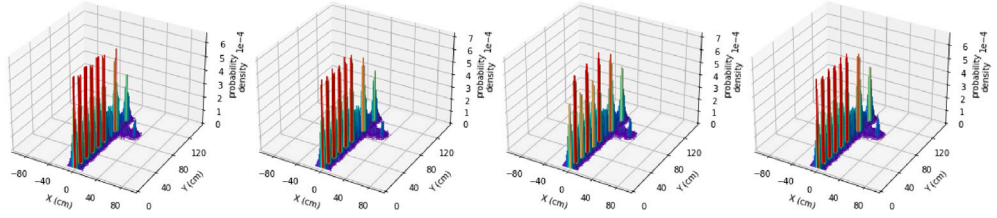 | | | |

## References


[1] Eurocode 5: Design of timber structures – Part 1-1: General – Common rules and rules for buildings: German version EN 1995-1-1:2004 + AC:2006 + A1:2008.

[2] H.J. Blaß, M. Schmid, Querzugfestigkeit von vollholz und brettschichtholz, Holz Als Roh- Und Werkst. 58 (6) (2001) 456–466, http://dx.doi.org/10.1007/s001070050460.

[3] M. Westermayr, F. Hunger, J.V.D. Kuilen, Strength and stiffness perpendicular to the grain of ash (fraxinus e.) and beech (fagus s.) in comparison to spruce (picea a.), in: V. Möttönen, E. Heinonen (Eds.), 6th International Scientific Conference on Hardwood Processing, in: Natural resources and bioeconomy studies, Natural Resources Institute Finland, Helsinki, 2017, URL https://www.semanticscholar.org/paper/Strength-and-stiffness-perpendicular-to-the-grain-Westermayr-Hunger/d45201ed9971b1b55b43a231bcbe22937a7c7ada.

[4] K. Möhler, H. Blumer, Gekruemmte Brettschichttraeger Mit Konstanter Querschnittschoehe Oder Mit Geneigtem Obergurt, Universität Karlsruhe (TH), 1978.

[5] J. Ehlbeck, K. Hemmer, 0Ber die tragfhhigkeit gekriimmter brettschichtholztrhger, Holz Als Roh- Und Werkst. 43 (1985) 375–379.

[6] S. Franke, B. Franke, A.M. Harte, Failure modes and reinforcement techniques for timber beams – state of the art, Constr. Build. Mater. 97 (2015) 2–13, http://dx.doi.org/10.1016/j.conbuildmat.2015.06.021.

[7] H.J. Blass, O. Eberhart, J. Ehlbeck, M. Gerold, Wirkungsweise von eingeleimten gewindestangen bei der aufnahme von querzugkräften in gekrümmten biegeträgern und entwicklung von bemessungsgrundlagen. Teil 3, 1996.

[8] J. Jönsson, Load carrying capacity of curved glulam beams reinforced with self-tapping screws, Holz Als Roh- Und Werkst. 63 (5) (2005) 342–346, http://dx.doi.org/10.1007/s00107-005-0016-5.

[9] J.G. Fueyo, J.A. Cabezas, M.P. Rubio, M. Domínguez, Reduction of perpendicular-to-grain stresses in the apex zone of curved beams using glued-in rods, Mater. Struct. 43 (4) (2010) 463–474, http://dx.doi.org/10.1617/s11527-009-9503-1.

[10] S. Gowda, A. Ranta-Maunus, Curved and Cambered Glulam Beams: Part 1. Short Term Load Tests, in: VTT tiedotteita-meddelanden-research notes, vol. 1500, Technical Research Centre of Finland, Espoo, Finland, 1993.

[11] S. Gowda, A. Ranta-Maunus, Curved and Cambered Glulam Beams: Part 2. Long Term Load Tests under Cyclically Varying Humidity, in: VTT tiedotteita-meddelanden-research notes, vol. 1500, Technical Research Centre of Finland, Espoo, Finland, 1993.

[12] E.C. Zhu, H.Z. Zhou, Simulation of residual stress in curved glulam beams during manufacturing, WCTE (2010).

[13] S. Ormarsson, Ó.V. Gíslason, Moisture-induced stresses in glulam frames, Eur. J. Wood Wood Prod. 74 (3) (2016) 307–318, http://dx.doi.org/10.1007/s00107-016-1006-5.

[14] L.P. Qiu, E.C. Zhu, J.W.G. van de Kuilen, Modeling crack propagation in wood by extended finite element method, Eur. J. Wood Wood Prod. 72 (2) (2014) 273–283, http://dx.doi.org/10.1007/s00107-013-0773-5.

[15] H. Zhou, E. Zhu, S. Fortino, T. Toratti, Modelling the hygrothermal stress in curved glulam beams, J. Strain Anal. Eng. Des. 45 (2) (2010) 129–140, http://dx.doi.org/10.1243/03093247JSA563.

[16] J.C.F. Walker, Primary Wood Processing: Principles and Practice, second ed., Springer, Dordrecht The Netherlands, 2006.

[17] J.R. Aira, T. Descamps, L. van Parys, L. Léoskool, Study of stress distribution and stress concentration factor in notched wood pieces with cohesive surfaces, Eur. J. Wood Wood Prod. 73 (3) (2015) 325–334, http://dx.doi.org/10.1007/s00107-015-0891-3.

[18] E. Sorin, J.-L. Coureau, M. Chaplain, Prediction of the ultimate load-carrying capacity of wooden notched beams with and without reinforcements using a splitting model, Constr. Build. Mater. 271 (2021) 121518, http://dx.doi.org/10.1016/j.conbuildmat.2020.121518.

[19] J.G. Zandbergs, F. Smith, Finite element fracture prediction for wood with knots and cross grain, Wood Fiber Sci. 20 (1) (1988) 97–106.

[20] P. Guindos, M. Guaita, A three-dimensional wood material model to simulate the behavior of wood with any type of knot at the macro-scale, Wood Sci. Technol. 47 (3) (2013) 585–599, http://dx.doi.org/10.1007/s00226-012-0517-4.

[21] M. Lukacevic, J. Füssl, Numerical simulation tool for wooden boards with a physically based approach to identify structural failure, Eur. J. Wood Wood Prod. 72 (4) (2014) 497–508, http://dx.doi.org/10.1007/s00107-014-0803-y.

[22] A. Khaloian Sarnaghi, J.W.G. van de Kuilen, An advanced virtual grading method for wood based on surface information of knots, Wood Sci. Technol. 53 (3) (2019) 535–557, http://dx.doi.org/10.1007/s00226-019-01089-w.

[23] R.O. Foschi, J.D. Barrett, Glued-laminated beam strength: A model, J. Struct. Div. 106 (8) (1980) 1735–1754, http://dx.doi.org/10.1061/JSDEAG.0005496.

[24] H.-L. Mistler, Querzug-bemessung von BSH-trägern nach EC 5 ein vergieich mit forschungsergebnissen, Holz Als Roh- Und Werkst. 56 (1) (1998) 51–59, http://dx.doi.org/10.1007/s001070050263.

[25] J. Ehlbeck, F. Colling, Biegefestigkeit von brettschichtholz in abhängigkeit von rohdichte, elsatizitätsmodul, ästigkeit und keilzinkung der lamellen, der lage der keilzinkung sowie von der trägerhöhe: Tech. Rep: Versuchsanstalt für stahl, holz und steine, universität fridericiana karlsruhe, 1987.

[26] H. Blass, Biegefestigkeit Von Brettschichtholz Aus Buche, in: Karlsruher Berichte zum Ingenieurholzbau, vol. 1, Univ.-Verl. Karlsruhe, Karlsruhe, 2005.

[27] G. Fink, Influence of varying material properties on the load-bearing capacity of glued laminated timber (Ph.D. thesis), ETH Zurich, 2014, http://dx.doi.org/10.3929/ETHZ-A-010108864.

[28] G. Kandler, J. Füssl, A probabilistic approach for the linear behaviour of glued laminated timber, Eng. Struct. 148 (2017) 673–685, http://dx.doi.org/10.1016/j.engstruct.2017.07.017.

[29] C. Tapia Camú, Variation of mechanical properties in oak boards and its effect on glued laminated timber (Ph.D. thesis), Eric Cuvillier and Universität Stuttgart.
[30] M.A. Bezabeh, G.T. Bitsuamlak, M. Popovski, S. Tesfamariam, Probabilistic serviceability-performance assessment of tall mass-timber buildings subjected to stochastic wind loads: Part I - structural design and wind tunnel testing, J. Wind Eng. Ind. Aerodyn. 181 (2018) 85–103, http://dx.doi.org/10.1016/j.jweia.2018.08.012.
[31] German third national forest inventory: Result database, 2022, URL https://bwi.info/start.aspx.
[32] W. Fang, Q. Zhao, Q. Cai, A. Eziz, G. Chen, Y. Feng, H. Zhang, J. Zhu, C. Ji, Z. Tang, J. Fang, The relationships among structure variables of larch forests in China, For. Ecosyst. 7 (1) (2020) http://dx.doi.org/10.1186/s40663-020-00273-w.
[33] R. Sharma, Z. Vacek, S. Vacek, M. Kučera, A nonlinear mixed-effects height-to-diameter ratio model for several tree species based on czech national forest inventory data, Forests 10 (1) (2019) 70, http://dx.doi.org/10.3390/f10010070.
[34] K. Panagiotis, D. Evangelia, M. Panagiotis, Testing non-linear height-diameter functions for three native trees of Greece on ICP forests level II plots, 2019, URL http://repository-theophrastus.ekt.gr/theophrastus/handle/20.500.12038/163.
[35] K. Spångberg, J. Arlinger, L. Wilhelmsson, S.S.-O. Lundqvist, Ö. Hedenberg, Taper functions for picea abies (l.) karst. and pinus sylvestris l. in Sweden, 2001.
[36] D.W. Ormerod, A simple bole model, For. Chron. (1973) 136–138.
[37] C. Torresan, F. Pelleri, M.C. Manetti, C. Becagli, C. Castaldi, M. Notarangelo, U. Chiavetta, Comparison of TLS against traditional surveying method for stem taper modelling. a case study in European beech (fagus sylvatica l.) forests of mount amiata, Ann. Silvic. Res. 46 (2) (2021) 128–140, http://dx.doi.org/10.12899/asr-2198.
[38] M.M. Hassani, F.K. Wittel, S. Hering, H.J. Herrmann, Rheological model for wood, Comput. Methods Appl. Mech. Engrg. 283 (2015) 1032–1060, http://dx.doi.org/10.1016/j.cma.2014.10.031.
[39] J. Pěnčík, Tests of wooden specimens from scots pine (pinus sylvestris) with the help of anisotropic plasticity material model, Drvna Ind. 66 (1) (2015) 27–33, http://dx.doi.org/10.5552/drind.2015.1362.
[40] J.R. Aira, F. Arriaga, G. Íñiguez-González, Determination of the elastic constants of scots pine (pinus sylvestris l.) wood by means of compression tests, Biosyst. Eng. 126 (2014) 12–22, http://dx.doi.org/10.1016/j.biosystemseng.2014.07.008.
[41] P. Obara, Verification of orthotropic model of wood, Arch. Civ. Eng. 64 (3) (2018) 31–44, http://dx.doi.org/10.2478/ace-2018-0027.
[42] E. Guntekin, S. Arkar, Influence of moisture content on elastic constants of scots pine wood subjected to compression, Drew. Pr. Naukowe. Doniesienia. Komun. 62 (204) (2019) http://dx.doi.org/10.12841/wood.1644-3985.220.09, URL https://agro.icm.edu.pl/agro/element/bwmeta1.element.agro-28ae63d1-285c-479c-8d9e-5c182e1fa014.
[43] P. Niemz, W.U. Sonderegger, Holzphysik: Eigenschaften, PrÜFung Und Kennwerte, 2., aktualisierte Auflage, Hanser, München, 2021, http://dx.doi.org/10.3139/9783446470101.
[44] M. Grimsel, Mechanisches Verhalten Von Holz: Struktur- Und Parameteridentifikation Eines Anisotropen Werkstoffes: Zugl.: Dresden, Techn. Univ., Diss., 1999, in: Dresdner Forschungen Maschinenwesen, vol. 1, w.e.b.-Univ.-Verl., Dresden, 1999.
[45] J. Bodig, B.A. Jayne, Mechanics of Wood and Wood Composites, Van Nostrand Reinhold, New York and London, 1982.
[46] H. Neuhaus, Elastizitätszahlen von fichtenholz in abhängigkeit von der holzfeuchtigkeit, 1981.
[47] Forest Products Laboratory, Wood Handbook—Wood As an Engineer- Ing Material: General Technical Report FPL-GTR-190, Madison, 2010.
[48] M. Humar, Wood Properties and Processing, MDPI - Multidisciplinary Digital Publishing Institute, Erscheinungsort nicht ermittelbar, 2020, URL https://directory.doabooks.org/handle/20.500.12854/62799.
[49] W. Wang, Optimization of larch timbering cross section based on finite element, ICST Trans. Scalable Inf. Syst. (2018) 172998, http://dx.doi.org/10.4108/eai.26-1-2022.172998.
[50] L. Qiu, Performance of Curved Glulam Beams under Load and Moisture Variations: Doctoral Dissertation, Harbin Institute of Technology, Harbin, China, 2015.